



# Image-guided synergistic photothermal therapy using photoresponsive imaging agent-loaded graphene-based nanosheets



Wenjun Miao <sup>a,1</sup>, Gayong Shim <sup>a,1</sup>, Gunwoo Kim <sup>b</sup>, Soondong Lee <sup>a</sup>, Hee-Jung Lee <sup>c</sup>, Young Bong Kim <sup>c</sup>, Youngro Byun <sup>b</sup>, Yu-Kyoung Oh <sup>a,\*</sup>

<sup>a</sup> College of Pharmacy and Research Institute of Pharmaceutical Sciences, Seoul National University, Seoul, Republic of Korea

<sup>b</sup> Department of Molecular Medicine and Biopharmaceutical Sciences, Graduate School of Convergence Science, Seoul National University, Seoul, Republic of Korea

<sup>c</sup> Department of Bio-industrial Technologies, Konkuk University, Seoul, Republic of Korea

## ARTICLE INFO

### Article history:

Received 23 October 2014

Received in revised form 17 February 2015

Accepted 20 May 2015

Available online 21 May 2015

### Keywords:

Image-guided photothermal therapy

Photoresponsive imaging agent

Indocyanine green

Reduced graphene oxide nanosheets

Theranostics

## ABSTRACT

We report the image-guided synergistic photothermal antitumor effects of photoresponsive near-infrared (NIR) imaging agent, indocyanine green (ICG), by loading onto hyaluronic acid-anchored, reduced graphene oxide (HArGO) nanosheets. Loading of ICG onto either rGO (ICG/rGO) or HArGO (ICG/HArGO) substantially improved the photostability of photoresponsive ICG upon NIR irradiation. After 1 min of irradiation, the NIR absorption peak of ICG almost disappeared whereas the peak of ICG on rGO or HArGO was retained even after 5 min of irradiation. Compared with plain rGO, HArGO provided greater cellular delivery of ICG and photothermal tumor cell-killing effects upon laser irradiation in CD44-positive KB cells. The temperature of cell suspensions treated with ICG/HArGO was 2.4-fold higher than that of cells treated with free ICG. Molecular imaging revealed that intravenously administered ICG/HArGO accumulated in KB tumor tissues higher than ICG/rGO or free ICG. Local temperatures in tumor tissues of laser-irradiated KB cell-bearing nude mice were highest in those intravenously administered ICG/HArGO, and were sufficient to trigger thermal-induced complete tumor ablation. Immunohistologically stained tumors also showed the highest percentages of apoptotic cells in the group treated with ICG/HArGO. These results suggest that photoresponsive ICG-loaded HArGO nanosheets could serve as a potential theranostic nano-platform for image-guided and synergistic photothermal antitumor therapy.

© 2015 Elsevier B.V. All rights reserved.

## 1. Introduction

Photothermal therapy (PTT) utilizes photoresponsive agents taken up by cells and the conversion of absorbed light into local heating to destroy malignant tissue [1]. PTT is considered a minimally invasive cancer treatment approach that is advantageous compared with conventional chemotherapy because its spatial and temporal controllability [2,3] limit side effects that commonly occur in chemotherapy owing to nonspecific drug delivery to all tissues, including healthy tissues. Multidrug resistance, an additional concern with chemotherapy that leads to treatment failure [4], can also be avoided by PTT because achieving ablative temperatures induces irreversible tissue necrosis [5].

Several types of photoresponsive dyes with maximal absorption peaks in the near-infrared (NIR) region have been explored as imaging agents [6]. Among them, the amphiphilic dye indocyanine green (ICG), is the only NIR imaging agent approved by the U.S. Food and Drug Administration, and used clinically for imaging retinal and choroidal

vasculatures, and guiding biopsies [7]. However, the use of ICG suffers dramatically from rapid, light-induced decomposition [8,9] and clearance, resulting in a plasma half-life of 2–4 min [10]. Thus, various modalities, including calcium phosphosilicate nanoparticles [11], superparamagnetic iron oxide nanoparticles [12], gold nanoparticles [13] and polymeric micelles [14], have been utilized to improve the photostability and prolong retention of ICG in the bloodstream.

Carbon-based nanomaterials, such as carbon nanotubes, graphenes and fullerenes, have been intensely investigated for photothermal therapy applications. On a per-mass basis, both carbon nanotubes and graphenes exhibit a larger extinction coefficient of NIR light absorption than gold nanomaterials, and consequently higher photothermal conversion efficiency [15]. Intravenously administered polyethylene glycol-conjugated graphene nanosheets exhibit ultrahigh tumor retention and good photothermal antitumor efficacy [16]. Recently, we demonstrated that the photothermal tumor ablation capacity of poloxamer 407-functionalized graphene nanosheets was superior to that of poloxamer 407-functionalized carbon nanotubes in a murine xenograft tumor model [17]. Although graphene-based nanosheets produce a photothermal effect on their own, reducing the injection dose by loading photoresponsive agents would be desirable from a safety

\* Corresponding author.

E-mail address: [ohyk@snu.ac.kr](mailto:ohyk@snu.ac.kr) (Y.-K. Oh).

<sup>1</sup> These authors equally contributed to this work.

perspective. Moreover, photoresponsive imaging agent-loaded graphene-based nanosheets may be applicable as theranostics for image-guided photothermal therapy.

In this study, we tested whether the loading of photoresponsive imaging agent onto graphene-based nanosheets could provide image-guided and synergistic photothermal anticancer effects. For image-guided photothermal therapy, ICG was loaded onto reduced graphene oxide nanosheets (rGO). To enhance tumor accumulation and image intensity of ICG, we used hyaluronic acid (HA)-modified rGO for ICG delivery.

## 2. Materials and methods

### 2.1. Synthesis of rGO nanosheets

Graphene oxide (GO) was prepared from graphite powder following a modified Hummer's method [12]. Briefly, graphite powder (0.5 g; Sigma-Aldrich, St. Louis, MO, USA) was added to cold H<sub>2</sub>SO<sub>4</sub> (23 ml). While this mixture was gradually stirred on ice, KMnO<sub>4</sub> (3 g) and NaNO<sub>3</sub> (0.5 g) were added slowly. The resulting mixture was further stirred for 1 h at 35 °C. Subsequently, 46 ml of triple-distilled water (TDW) was added and the mixture was incubated at 90 °C for 1 h. The reaction was halted by adding 140 ml of TDW and 10 ml of 30% H<sub>2</sub>O<sub>2</sub>. The reaction product was washed and purified by repeated centrifugation, first with an aqueous 5% HCl solution and then with TDW (three times). Finally, the product was suspended in TDW and sonicated for 2 h to exfoliate the GO layers into GO nanosheets. Unexfoliated GO was removed by centrifugation at 1600 ×g for 10 min. The supernatant containing GO nanosheets was collected and filtered through 0.2-μm polycarbonate membrane filters (Millipore Corp., Billerica, MA, USA) using an extruder (Northern Lipid, British Columbia, Canada).

GO nanosheets were subsequently reduced to generate rGO nanosheets according to the method of Li and colleagues [18], with slight modification. In brief, 2.0 ml of GO nanosheets (5 mg/ml) in TDW was mixed with a solution containing 8.0 ml of TDW, 0.5 ml of ammonia solution (28 wt.% in water; Junsei Chemical, Tokyo, Japan) and 5.0 μl of hydrazine monohydrate (64 wt.% in water, Sigma-Aldrich). The resultant mixture was stirred at 80 °C for 10 min. After cooling the mixture to room temperature, excess hydrazine and ammonia were removed by dialysis (MWCO 100 K; Spectrum Laboratories, Inc., Rancho Dominguez, CA, USA) against TDW. The resulting rGO nanosheets were stored at 4 °C until use.

### 2.2. Synthesis of HARGO nanosheets

To modify the surface of rGO with HA, cholesteryl HA (CHA) was synthesized by linking the amino group of cholesteryl-2-aminoethylcarbamate (CAEC) with the carboxyl group of HA according to a previous method [19]. The synthesis of CAEC was confirmed by proton nuclear magnetic resonance (<sup>1</sup>H NMR) spectroscopy using a Bruker Avance-500 MHz FT-NMR spectrometer (Bruker, Billerica, MA, USA). The molecular weight of CAEC was measured by electrospray ionization (ESI) mass spectrometry using a Finnigan Mat LcQ mass spectrometer (Thermo Fisher Scientific, Inc., Waltham, MA, USA). Before the condensation reaction with CAEC, HA (214 kDa; Lifecore Biomedical, Chaska, MN, USA) was converted to its tetrabutylammonium salt (HA-TBA). After dissolving 100 mg of HA-TBA in 10 ml of dimethyl sulfoxide, 0.33 ml of CAEC (20 mg/ml) in a mixture of dichloromethane and methanol (1:1, v/v) was added to the solution, followed by addition of 4.2 mg of 4-(4,6-dimethoxy-1,3,5-triazin-2-yl)-4-methylmorpholinium chloride (Alfa Aesar, Ward Hill, MA, USA) in 0.5 ml of dimethyl sulfoxide. The resulting CHA was stored at 4 °C until use. For surface coating with CHA, an aqueous solution of rGO nanosheets in TDW (1 mg/ml) was mixed with an equal volume of CHA solution (2 mg/ml). After sonication for 30 min, the mixture was dialyzed (MWCO 1000 K; Spectrum

Laboratories, Inc.) against TDW for 24 h to remove excess free CHA to yield purified HARGO nanosheets.

### 2.3. Animals

In vivo experiments were conducted using 5-weeks-old female Balb/c or Balb/c athymic nude mice with 18–20 g body weight (Orient Bio Inc., Seungnam, Republic of Korea; approved animal experimental protocol number SNU-130129-3-1). The animals were raised under standard pathogen-free conditions at the Animal Center for Pharmaceutical Research at Seoul National University. All animal experiments were conducted in accordance with the Guidelines for the Care and Use of Laboratory Animals of the Institute of Laboratory Animal Resources, Seoul National University.

### 2.4. Loading of ICG onto nanosheets

ICG-loaded rGO (ICG/rGO) and ICG-loaded HARGO (ICG/HARGO) nanosheets were prepared by adding ICG to rGO nanosheets in plain or HA-coated form at a weight ratio of 1:5. Free ICG was removed using a PD-10 desalting column (GE Healthcare, Buckinghamshire, UK). The stability of rGO and HARGO nanosheets, with and without ICG loading, was tested in phosphate buffered saline (PBS; 150 mM, pH 7.4). An aliquot (0.2 ml) of test samples in TDW was added to 0.8 ml of PBS, and the solutions were allowed to stand for 7 d. The stability of ICG/HARGO nanosheets was evaluated during this period by monitoring the mixtures for the appearance of precipitates using a digital camera (Canon PC1089; Canon Inc, Tokyo, Japan).

### 2.5. Size and zeta potential measurements

The morphology of rGO or HARGO nanosheets was examined by transmission electron microscopy (TEM) using a JEM1010 system (JEOL Ltd, Tokyo, Japan). The hydrodynamic diameters and lateral dimensions of nanosheets were determined by dynamic light scattering using a He-Ne laser (10 mW). Zeta potential values of nanosheets (diluted in TDW), with or without ICG loading, were determined by laser Doppler microelectrophoresis at an angle of 22° using an ELS-8000 instrument (Photal, Osaka, Japan).

### 2.6. Fluorescence measurement of ICG upon complexation and NIR irradiation

The fluorescence intensity of ICG upon complexation and NIR irradiation was measured in various conditions. ICG (5 μM) on nanosheets was incubated at 37 °C for 5 min in 1 ml of TDW, RPMI-1640 medium (Gibco-BRL Life Technologies, Carlsbad, CA, USA), or murine serum from 5-wk-old female Balb/c (Orient Bio Inc.). In some experiments, ICG (5 μM) on nanosheets was irradiated for 3 min using 808 nm continuous wave NIR diode laser beam (BWT Beijing LTD, Beijing, China) with an output power of 1.2 W. As a control, free ICG (5 μM) in TDW was used. The fluorescence intensity of ICG in each sample was then measured using an eXplore Optix system (Advanced Research Technologies Inc., Montreal, Canada). A 785 nm pulsed-laser diode was used to excite ICG.

### 2.7. Detection of photothermal properties upon irradiation

Photothermal properties were measured using an IR thermal imaging system after irradiation of each sample. ICG (1.3 μM) in free form or on nanosheets (5 μg/ml of rGO) were irradiated using an 808 nm continuous wave NIR diode laser beam (BWT Beijing LTD) with an output power of 1.2 W. The temperature and photothermal images of the suspensions during laser irradiation were recorded every 30 s using an IR thermal imaging system (FLIR T420; FLIR Systems Inc., Danderyd, Sweden). The photothermal heating curve of TDW was measured as a negative control.

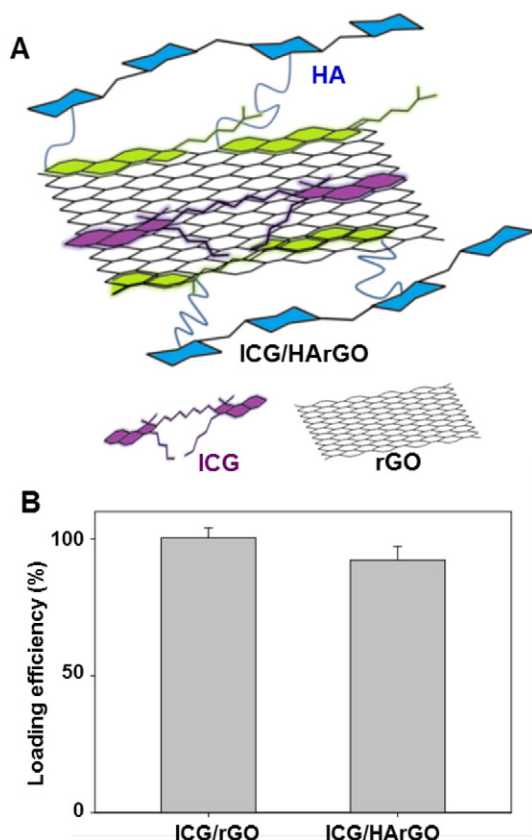


**Fig. 1.** Scheme and loading efficiencies of ICG on rGO. (A) A schematic illustration of ICG/HArGO. (B) The loading efficiency of ICG on rGO or HArGO was measured using UV/vis spectrophotometry.

### 2.8. Singlet oxygen generation upon irradiation

Production of singlet oxygen ( $^1O_2$ ) was measured using a singlet oxygen sensor green reagent (SOSG, Life Technologies, Grand Island, NY, USA) after irradiation of each sample. ICG (1.3  $\mu$ M) in free form or on nanosheets (5  $\mu$ g/ml) was irradiated using an 808 nm continuous wave NIR diode laser beam (BWT Beijing LTD) with an output power of 1.2 W. During laser irradiation, 50  $\mu$ l of aliquot was minutely collected from 1 ml of each sample. Each aliquot was mixed with 2.5  $\mu$ M of SOSG solution. The presence of singlet oxygen was detected by fluorescence of SOSG with its excitation/emission of 504/525 nm using a fluorescence microplate reader (Gemini XS; Molecular Device, Sunnyvale, CA, USA).

### 2.9. In vitro photothermal effect of ICG/HArGO following NIR irradiation

Human KB epidermal carcinoma cells (American Type Culture Collection, Rockville, MD, USA) were cultured in RPMI-1640 medium (Gibco-BRL Life Technologies, Carlsbad, CA, USA) supplemented with 10% fetal bovine serum, 100 units/ml penicillin, and 100  $\mu$ g/ml streptomycin (complete RPMI-1640 media). KB cells were seeded onto 12-well plates at a density of  $1 \times 10^5$  cell/well. The following day, cells were treated with free ICG, rGO, ICG/rGO, HArGO, or ICG/HArGO at an ICG concentration of 5.2  $\mu$ M and a nanosheet concentration of 20  $\mu$ g/ml. After 24 h of incubation at 37  $^{\circ}$ C, the cell suspensions were centrifuged at 200  $\times$ g for 3 min to evaluate the cellular uptake of rGO nanosheets. The black color of cell pellets was monitored using a digital camera (Canon PC1089). The cell suspensions were irradiated with an 808 nm continuous-wave NIR diode laser at an output power of 1.2 W. The temperature and photothermal images of the cell suspensions during laser irradiation were recorded minutely using an IR thermal imaging system

(FLIR T420). Immediately after irradiation, cell viability was quantified using a Cell Counting Kit-8 (CCK8) according to the protocol provided by the manufacturer (Dojindo Molecular Technologies, Inc., Rockville, MD, USA). Cell viability was expressed as a percentage of that measured in control groups.

### 2.10. Single acute toxicity study

For acute toxicity test, 5-week-old female Balb/c mice (Orient Bio Inc.) were intravenously administered with various doses of rGO, HArGO, or ICG/HArGO nanosheets. For isotonicity, the nanosheets were dispersed in 5% glucose solution. One day after intravenous bolus injection into the tail veins of female Balb/c mice, the survival of mice was recorded.

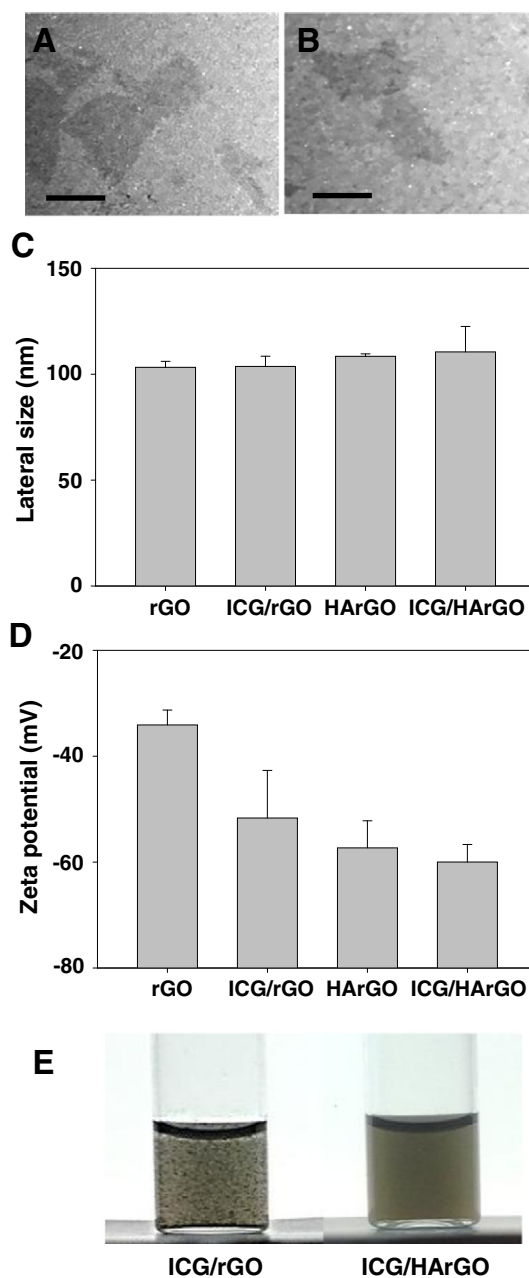


**Fig. 2.** Characterization of ICG/HArGO. TEM images of ICG/rGO (A) and ICG/HArGO (B). (C) The lateral diameters of rGO, ICG/rGO, HArGO, and ICG/HArGO, measured by dynamic light scattering. (D) Zeta potentials, determined using an electro-Doppler method. (E) Stability of ICG/rGO and ICG/HArGO nanosheet suspensions in PBS. Scale bars = 100 nm.

### 2.11. Molecular imaging of ICG

Molecular whole body imaging was used to trace the distribution of ICG in KB tumor-bearing mice. Five week old athymic nude mice (Orient Bio, Inc.) were subcutaneously injected at the dorsal right side with  $2 \times 10^6$  KB cells. When the tumor volume reached 80–100 mm<sup>3</sup>, the mice were subjected to intravenous administration of free ICG, ICG/rGO, ICG/HArGO at the rGO dose of 5 mg/kg, and the ICG dose of 1 mg/kg. At various time points post-dose, the images of ICG were assessed using an eXplore Optix system (Advanced Research Technologies Inc.). In some experiments, mice were sacrificed at 1 and 24 h post-dose, and major organs were extracted for ex vivo imaging.

### 2.12. In vivo photothermal study

The photothermal anticancer effects of ICG/HArGO were tested using KB tumor-bearing nude mice. Five-week-old athymic nude mice (Orient Bio Inc.) were subcutaneously injected at the dorsal right side with  $2 \times 10^6$  KB cells. When tumor volumes reached 80–100 mm<sup>3</sup>, mice were intravenously administered with 1 mg/kg of ICG in free form or on nanosheets (5 mg/kg). One day post-administration, the tumor sites of mice were irradiated for 3 min with an 808 nm continuous wave NIR laser at an output power of 1.2 W. Light-induced temperature changes in the tumor region were recorded using an FLIR T420 real-time IR thermal imaging system. Tumor volume was calculated according to the equation  $a \times b^2 \times 0.5$ , where  $a$  is the largest and  $b$  is the smallest dimension. In some experiments, tumor tissues were extracted on day 26 after the first inoculation of tumor cells, fixed in 10% neutral buffered formalin, and embedded in paraffin blocks. Tumor tissue sections (4  $\mu$ m thick) were immunostained with an anti-proliferating cell nuclear antigen (PCNA) antibody (Thermo Fisher Scientific) by terminal deoxynucleotidyl transferase dUTP nick-end labeling (TUNEL) (Millipore Corporation). The numbers of proliferating and apoptotic cells were counted using Image-Pro Plus Version 6.0 image analysis software (Media Cybernetics, Inc., Rockville, MD, USA) using an Eclipse TE2000-S microscope (Nikon, Tokyo, Japan) [20].

### 2.13. Statistics

Analysis of variance (ANOVA) with post hoc Student–Newman–Keuls test was used for statistical evaluation of experimental data. All statistical analyses were done using SigmaStat software (version 3.5; Systat Software, Richmond, CA, USA). A  $p$ -value < 0.05 was considered statistically significant.

## 3. Results

### 3.1. Characterization of ICG/HArGO

ICG was loaded onto the surfaces of rGO or HArGO nanosheets via  $\pi$ – $\pi$  interaction, as illustrated in Fig. 1A. The loading efficiencies of ICG on rGO and HArGO nanosheets were  $100.4\% \pm 3.6\%$  and  $92.3\% \pm 5.0\%$ , respectively (Fig. 1B). The morphology of ICG/rGO (Fig. 2A) did not differ from that of ICG/HArGO (Fig. 2B). The loading of ICG did not significantly affect the sizes of rGO or HArGO (Fig. 2C). The zeta potential values of nanosheets decreased after loading of ICG onto rGO (Fig. 2D). Immediately after dispersion in PBS, aggregates formed in the ICG/rGO suspension, but not in the ICG/HArGO suspension (Fig. 2E).

Upon complexation onto nanosheets, the fluorescence of ICG was significantly quenched. Although the intensity of free ICG in TDW was  $1057.7 \pm 143.5$ , the intensity values of ICG on rGO and HArGO in TDW were  $2.1 \pm 0.3$  and  $12.2 \pm 1.4$  (Fig. 3A). The substantial quenching of ICG upon complexation onto nanosheets was similarly observed in RPMI-1640 media (Fig. 3B), and serum (Fig. 3C). Moreover, the complexation onto nanosheets increased the photostability of ICG. After NIR irradiation, the intensity of free ICG was decreased in TDW (Fig. 3A),

RPMI-1640 media (Fig. 3B), and serum (Fig. 3C). In contrast, the intensity of ICG on rGO or HArGO did not significantly change upon NIR irradiation in the environments tested in this study.

### 3.2. Thermal conductivity and photostability of ICG on nanosheets

The thermal conductivity and photostability of ICG on nanosheets were different compared with those of free ICG. Upon laser irradiation, free ICG solution showed the increase of temperature, similar to TDW alone (Fig. 4A, B). After 1, 2, and 5 min of irradiation, the temperature increase for free ICG was  $2.3 \pm 0.3$  °C,  $3.4 \pm 0.2$  °C, and  $4.2 \pm 0.3$  °C, respectively (Fig. 4A). The thermal conductivity of rGO and HArGO was higher than that of free ICG, with both nanosheet preparations exhibiting a gradual temperature increase that was proportional to the irradiation time. After 5 min of irradiation, the temperature

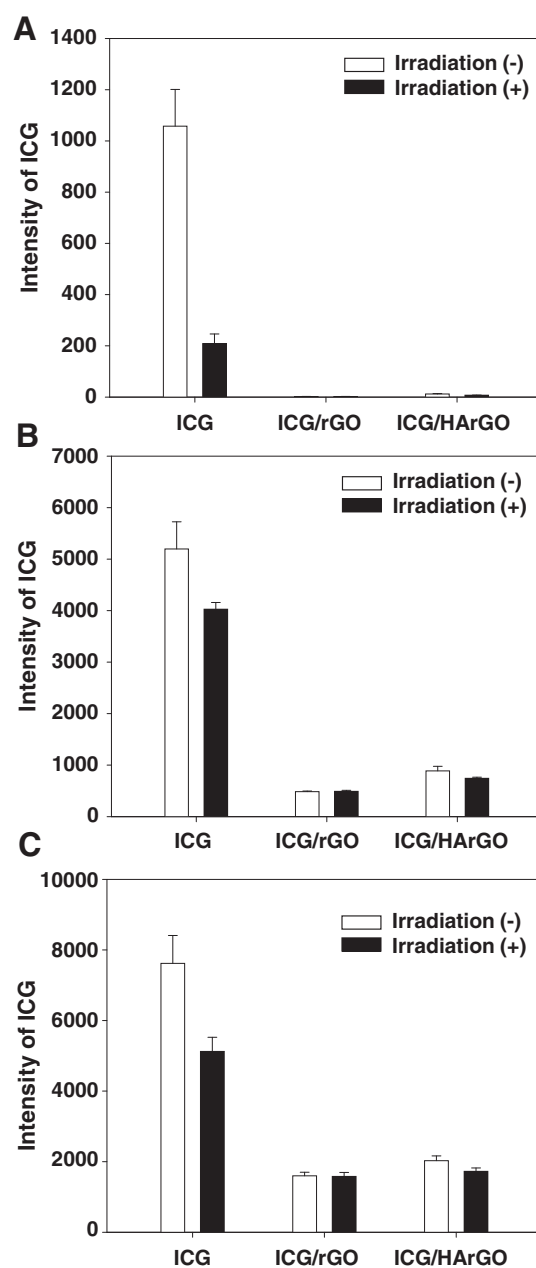


**Fig. 3.** Quenching and photostability of ICG on nanosheets. The intensity of ICG on rGO or HArGO was measured in TDW (A), RPMI-1640 media (B), or serum (C) before and after laser irradiation.

increase for rGO and HArGO was  $15.1\text{ }^{\circ}\text{C} \pm 0.3\text{ }^{\circ}\text{C}$  and  $14.5\text{ }^{\circ}\text{C} \pm 0.4\text{ }^{\circ}\text{C}$ , respectively. Unlike free ICG, ICG on nanosheets displayed a continuous increase in temperature with increased irradiation time. After 5 min of irradiation, the temperature increase for ICG/rGO and ICG/HArGO was  $23.6\text{ }^{\circ}\text{C} \pm 0.8\text{ }^{\circ}\text{C}$  and  $23.4\text{ }^{\circ}\text{C} \pm 0.6\text{ }^{\circ}\text{C}$ , respectively. Photostability significantly differed between ICG in free form and on nanosheets. UV spectra of free ICG revealed a rapid loss of the NIR absorption peak of free ICG upon irradiation. After 1 min of irradiation, the NIR absorption peak of ICG almost disappeared (Fig. 4C). In contrast, the NIR absorption peak of ICG on rGO (Fig. 4D) or HArGO (Fig. 4E) was retained, even after 5 min of irradiation. As compared to free ICG, ICG on nanosheets showed significantly lower singlet oxygen generation upon irradiation. Singlet oxygen was rapidly generated from free ICG during NIR irradiation (Fig. 4F). In contrast, the production of singlet oxygen was not observed in ICG-loaded rGO (Fig. 4G) or HArGO (Fig. 4H) during 5 min of irradiation.

### 3.3. Cellular uptake and photothermal antitumor effects of ICG delivered using ICG/HArGO nanosheets

Although ICG/rGO and ICG/HArGO showed similar thermal conductivity (Fig. 4A, B), they differed in cellular uptake and in vitro photothermal antitumor effects. Pellets of KB cells treated with HArGO or ICG/HArGO were a more dense black color than those treated with rGO or ICG/rGO (Fig. 5A). The increase in the temperature of cell pellets after irradiation depended on HA and ICG on rGO nanosheets. The irradiation-sensitive

temperature increase was highest in the group treated with ICG/HArGO, followed by HArGO, ICG/rGO, rGO, and free ICG (Fig. 5A, B). Real-time IR thermal imaging showed that the temperature of cell suspensions treated with ICG/HArGO was  $77.8\text{ }^{\circ}\text{C} \pm 2.3\text{ }^{\circ}\text{C}$  after 3 min of irradiation, a temperature that was 2.4-fold higher than that of cells treated with free ICG (Fig. 5B). In the absence of NIR irradiation, no group showed significant killing of KB cells (Fig. 5C). However, after 3 min of NIR irradiation, only treatment with ICG/HArGO killed more than 90% of KB cells.

### 3.4. Safety profiles of ICG delivered using nanosheets

The safety profiles of HArGO nanosheets differed from those of rGO nanosheets (Fig. 6). Following treatment with rGO nanosheets, the survival rate was 40% at the dose of 20 mg/kg and decreased to 0% at the doses of 40 mg/kg. Unlike rGO nanosheet-treated group, both HArGO nanosheet-treated group and ICG/HArGO-treated group showed 100% of survival even at a dose of 50 mg/kg.

### 3.5. In vivo images of ICG delivered using nanosheets

Images of ICG in KB tumor-bearing mice differed among various formulations. One hour after intravenous administration, free ICG was mainly distributed to the liver (Fig. 7A and B). The imaging data show that the distribution of free ICG to the liver decreased with time (Fig. 7A, C). The mean photon counts of free ICG to the liver were 55.7- and 4.3-fold higher than those to the tumor tissues at 1 h (Fig. 7D)

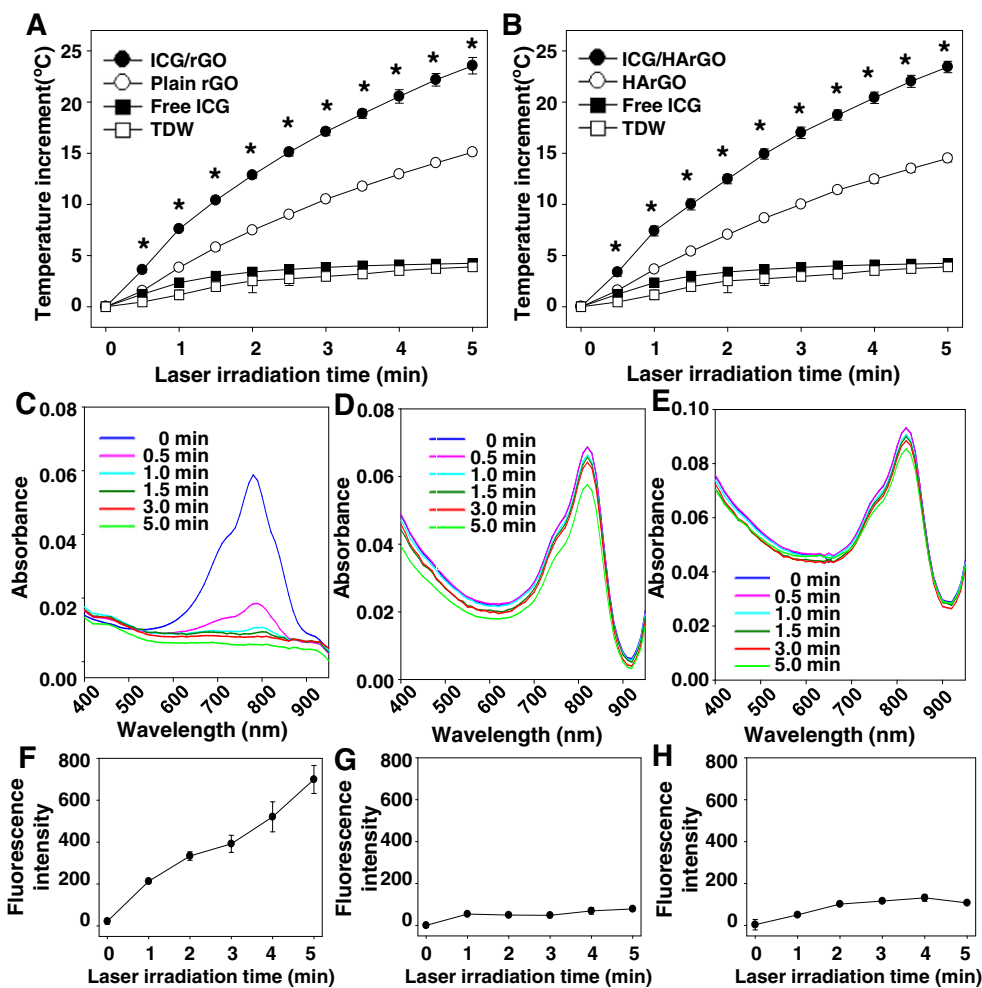
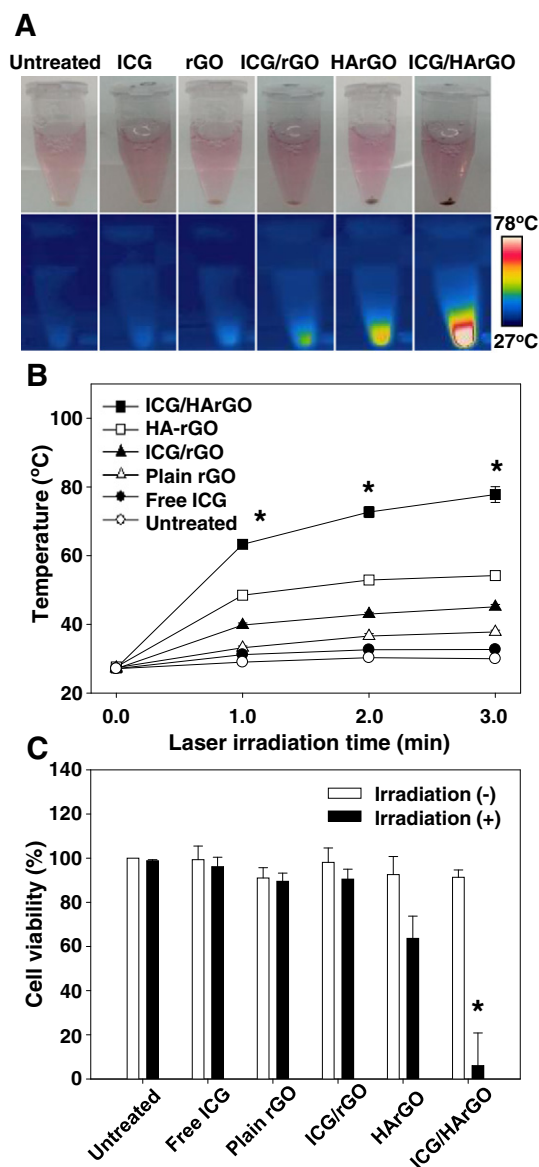


Fig. 4. Photothermal capacity of the ICG/HArGO. Irradiation with an 808 nm laser increases the temperature of ICG/rGO (A) and ICG/HArGO (B) suspensions, as measured using real-time IR thermal imaging techniques. (C–E) The UV absorbance spectrum of free ICG (C), ICG/rGO (D), and ICG/HArGO (E) was measured after different laser irradiation times. Production of singlet oxygen from free ICG (F), ICG/rGO (G), and ICG/HArGO was observed during laser irradiation. \* $p < 0.05$  compared to other groups (ANOVA and Student–Newman–Keuls test;  $n = 4$ ).

and 48 h (Fig. 7E) post-dose, respectively. Unlike free ICG, ICG complexed with rGO or HArGO showed the higher photon counts in the tumor tissues relative to the liver at 48 h post-dose. In case of rGO complexation, the mean photon count of ICG at the tumor tissues was 12.1-fold higher than that at the liver at 48 h post-dose (Fig. 7E). Following ICG on HArGO administration, the photon count of ICG at the tumor tissues was 47.7-fold higher than that at the liver at 48 h post-dose (Fig. 7E).

### 3.6. Image-guided photothermal effect of ICG/HArGO nanosheets

As the locations of tumor tissues were visualized by ICG through molecular imaging, NIR was irradiated onto the tumor tissues and temperature increases at the tumor sites were monitored by IR thermal imaging (Fig. 8). One day post-treatment, the highest temperature was observed in the tumor tissues of the group treated with ICG/HArGO after 3 min of NIR laser irradiation (Fig. 8A). In the ICG/HArGO-treated



**Fig. 5.** Photothermal antitumor effect of ICG/HArGO. KB cells were left untreated or were treated with free ICG, rGO, ICG/rGO, HArGO, or ICG/HArGO. After 24 h, the appearances and real-time temperature increases of pellets upon irradiation were assessed, and cell viability was measured. (A) Appearance and temperature of cell pellets upon irradiation. (B) Highest cell suspension temperature, determined using FLIR QuickReport 1.2 software. (C) Cell viability was measured using the CCK8 assay. \* $p < 0.05$  compared to other groups (ANOVA and Student–Newman–Keuls test;  $n = 4$ ).

group, the temperature at the tumor site was  $49.4 \pm 1.0 \text{ }^\circ\text{C}$ , a temperature that was  $9.0 \text{ }^\circ\text{C}$  and  $9.2 \text{ }^\circ\text{C}$  higher than that for ICG/rGO and free ICG-treated groups, respectively (Fig. 8B).

### 3.7. Synergistic photothermal antitumor effect of ICG/HArGO after image-guided irradiation

In vivo photothermal antitumor efficacy was improved by delivery of ICG using HArGO nanosheets. Following a single NIR treatment on day 7, tumor cell growth rate remained high in mice administered free ICG, rGO, ICG/rGO, or HArGO (Fig. 9A, C) and their tumors reached volumes greater than  $2300 \text{ mm}^3$  on day 26 after inoculation (Fig. 9B). Mice treated with ICG/HArGO responded differently to irradiation. One day after NIR irradiation (day 8), tumor sites were covered with a black scab. By day 26, the scab had almost completely detached with complete eradication of the tumor mass (Fig. 9B, C).

Tumor cell proliferation and apoptosis were evaluated by immunohistochemistry (Fig. 10). The number of PCNA-positive cells in tumor tissues was significantly lower in the group treated with ICG/HArGO compared with other treatment groups (Fig. 10A, C). TUNEL assays also showed that the percentage of apoptotic cells in tumor tissue was highest in the ICG/HArGO-treated group (Fig. 10B, D), where the number of apoptotic cells was 20.8-fold and 61.6-fold higher than that in the free ICG-treated group and untreated group, respectively (Fig. 10D).

## 4. Discussion

Here, we demonstrated that HArGO could substantially increase the photostability and photothermal antitumor potency of ICG. ICG in free form suffers from photo-induced decomposition after NIR laser irradiation. However, by loading onto rGO or HArGO nanosheets, ICG retained its photostability after NIR laser irradiation. Although ICG/rGO and ICG/HArGO showed similar thermal conductivity in vitro, ICG/HArGO showed a greater photothermal effect at the cell level and in tumor-bearing mice by virtue of CD44 receptor-mediated delivery.

Unlike free ICG, whose NIR absorption peak rapidly disappeared (1 min) after NIR irradiation, ICG on rGO or HArGO nanosheets retained its photostability and responded to NIR irradiation for more than 5 min (Fig. 4D, E). These results are consistent with previous reports that ICG rapidly decomposes into small fragments upon absorbing light energy [21]. This instability of ICG to light has limited its utility, restricting it to use as a fluorescence imaging agent or photothermal absorber.

We observed that the fluorescence of ICG was quenched upon complexation onto rGO or HArGO nanosheet. Similar to our observation,

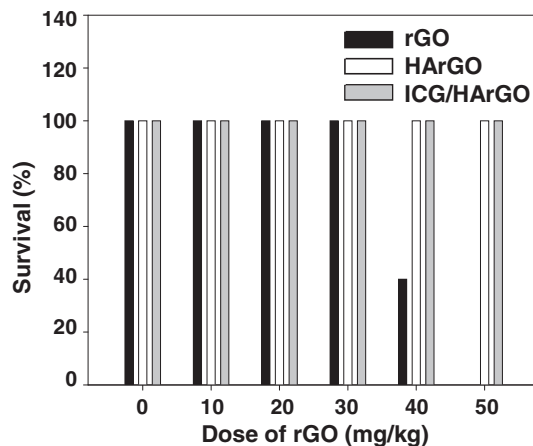


**Fig. 6.** In vivo safety of rGO and HArGO nanosheets. Balb/c mice were intravenously injected with various doses of rGO, HArGO, or ICG/HArGO nanosheets ( $n = 5$ ), and survival was assessed 1 day later.

a recent study reported the quenching of ICG by complexation with GO [22]. In our previous study, the quenching of fluorescence was observed after complexation with GO nanosheets. Moreover, we observed the quenching of ICG on rGO or HArGO nanosheets in serum. The lack of dequenching in the serum condition indicates that ICG complexation on nanosheets was stable in body fluid conditions.

The photostability of ICG was enhanced by complexation with rGO or HArGO nanosheets in serum (Fig. 3). The increased photostability of ICG on nanosheets can be in part explained by the graphene-mediated quenching of electron donors, singlet oxygen (Fig. 4G, H) [23,24]. It has been reported that singlet oxygen could catalyze the photo-induced decomposition of ICG (Fig. 4F) [9]. The quenching of electron donors by rGO or HArGO nanosheets may consume the destabilizer and lead to increase the stability of complexed ICG upon irradiation.

We observed that the tumor signal of ICG was the highest after delivery of ICG in HArGO complexes (Fig. 7). The lack of dequenching in serum and under irradiation (Fig. 4) supports that it is unlikely that ICG is released out from nanosheets during circulation or under heating conditions. The tumor-specifically enhanced fluorescence signal of ICG would be thus due to the liberation of ICG from nanosheets in tumor microenvironments, rather than the accumulation of quenched ICG/HArGO complexes. After taken up by the tumor cells, fluorescence

molecules have been shown to be released from rGO nanosheets, and to recover their own fluorescence [20,25]. In our previous study, we found the dequenching of chlorin e6 inside tumor cells 1 h after treatment with quenched chlorin e6 on GO complexes [25]. The enhanced image intensity of ICG given on HArGO at tumor tissues could guide the exact tumor locations in NIR irradiation for photothermal therapy.

The efficacy of ICG in photothermally ablating tumors in vivo was greatest in KB tumor-bearing mice treated with ICG/HArGO. The greater distribution of ICG/HArGO to the tumor tissue probably contributes to this enhanced photothermal effect. This notion is supported by our observation that the intensity of ICG-derived images (Fig. 7) and local tumor tissue temperature were highest in the group treated with ICG/HArGO (Fig. 8A). Since the thermal conductivity of both ICG/rGO and ICG/HArGO was similar in vitro, it is likely that the higher temperature is due to the greater distribution of ICG/HArGO to tumor tissues. This is consistent with the previous report that HA derivative-coated carbon nanotubes more effectively distribute to HA receptor-overexpressing tumor tissue [26,27].

Although HArGO treatment increased the temperature of cells up to 43 °C upon NIR irradiation in vitro (Fig. 8), it did not significantly reduce the growth of tumor tissues (Fig. 9). The lack of antitumor effect by HArGO treatment upon NIR irradiation can be explained by the

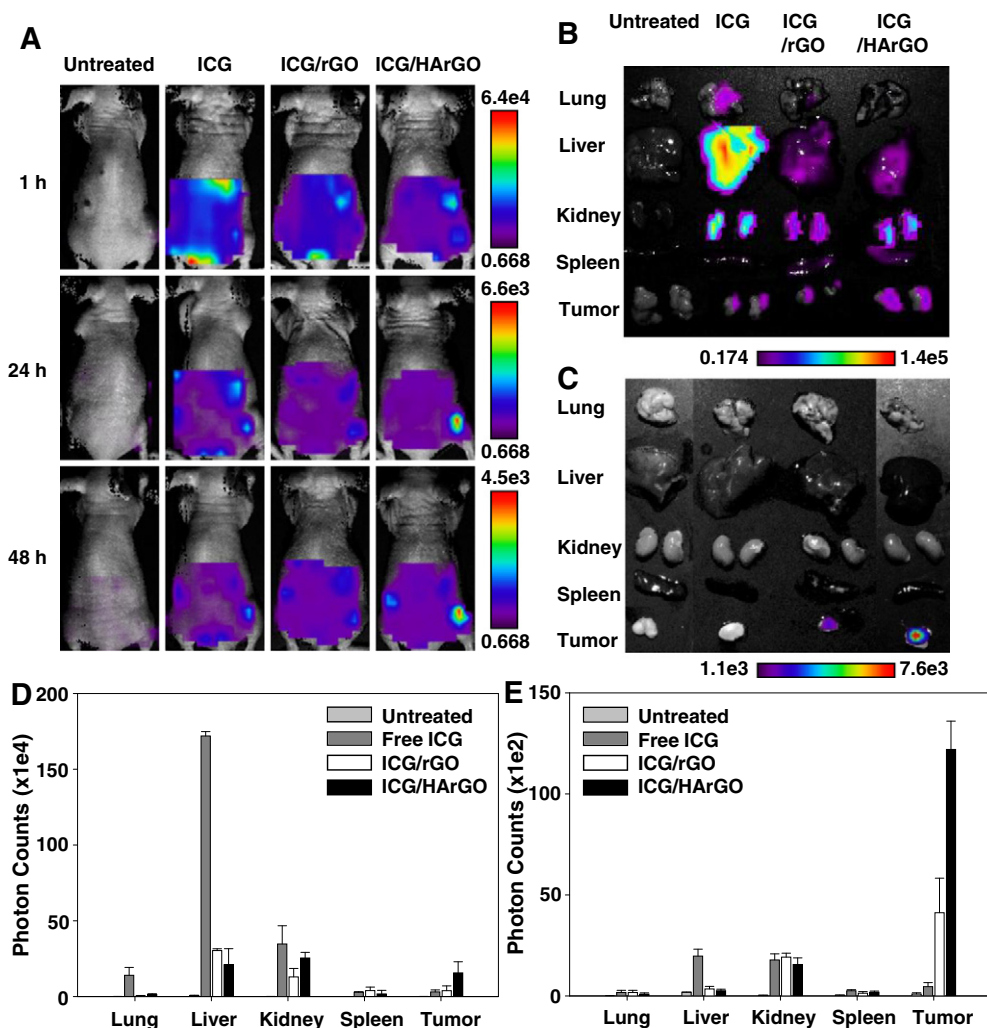


**Fig. 7.** Molecular images of ICG in tumor-bearing mice. KB-bearing mice were systemically treated with free ICG, ICG/rGO, or ICG/HArGO (ICG 1 mg/kg). After 1 h, 24 h, and 48 h (A), the images of ICG-accumulated tissues were visualized using a molecular imaging system. For ex vivo imaging, lung, liver, kidney, spleen, and tumor tissues were visualized (B, C) and photon counts were measured (D, E) at 1 h (B, D) or 48 h (C, E) post-dose. The result are the mean  $\pm$  SD of four independent experiments. \*Significantly higher ( $p < 0.05$ ) compared to the other groups (assessed by ANOVA and the Student–Newman–Keuls test).

insufficient duration of hyperthermia. When mice were treated with HArGO, the temperatures of tumor tissues increased with irradiation, and reached over 40 °C. However, after cessation of irradiation, the temperature decreased immediately lower than 40 °C (Suppl. Fig. 1D). As compared to HArGO, ICG/HArGO showed the prolonged retention of hyperthermia over 3 min (Suppl. Fig. 1D). It has been reported that the temperature of cells should be maintained over 43 °C for several minutes to trigger hyperthermia-induced cell apoptosis [28,29]. Moreover, our *in vitro* study revealed that the elevation of temperature to 43 °C for 2 min did not significantly reduce the viability of ICG/rGO-treated cells (Fig. 5).

In mice treated with ICG/HArGO, irradiation increased the temperature in tumor tissues to 49.4 °C, an increase not observed in any other treatment groups (Fig. 8). Cellular damage is known to occur when temperature is increased to 50–52 °C for 4–6 min, an effect attributable to the denaturation of proteins [30]. Thus, the photothermal activity of ICG/HArGO could result from the rapid local heating of the tumor up to an ablative temperature and induction of irreversible cell death. We observed that ICG/HArGO alone did not affect cell viability in the absence of irradiation (Fig. 5C). Based on the lack of *in vitro* anticancer activity of ICH/HArGO, it is unlikely that the *in vivo* tumor ablation effect of ICG/HArGO upon irradiation can be contributed by the antitumor effect of ICG/HArGO itself.

Although this study tested photolabile ICG as an imaging agent for loading onto HArGO, HArGO might be further developed for image-guided photothermal therapy of other photolabile, photoresponsive imaging agents, such as the cyanine dyes IR-125, IR-806 [31], and FS-308 [32]. In addition to enhancing the photostability of such photolabile and photoresponsive imaging agents, the photothermal property of HArGO per se could augment the potency of image-guided photothermal therapy. Moreover, the loading of photothermal agents could reduce the dose of HArGO required while improving therapeutic outcomes.

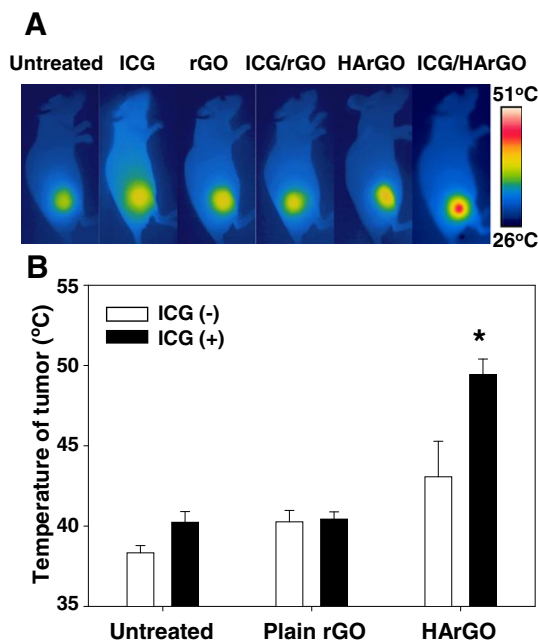


**Fig. 8.** Photothermal effect of the ICG/HArGO after image-guided irradiation. KB-bearing mice were injected intravenously with free ICG, rGO, ICG/rGO, HArGO, or ICG/HArGO. Immediately after irradiation with an 808-nm laser, real-time temperature changes at the tumor site were visualized by real-time IR thermal imaging (A), and the average temperature of the tumor site was measured using FLIR QuickReport 1.2 software (B). \* $p < 0.05$  compared to other groups (assessed by the ANOVA and Student–Newman–Keuls test;  $n = 5$ ).

## 5. Conclusions

Our results suggest the potential of ICG/HArGO for image-guided synergistic photothermal antitumor therapy. Loading of the photolabile ICG onto HArGO nanosheets could stabilize ICG upon NIR irradiation for photothermal effect. The endogenous photothermal properties of HArGO nanosheets can be exploited to synergistically enhance photothermal activity through loading of photoresponsive imaging agents. In addition, the tumor-specifically activated image intensity of ICG delivered by the HArGO can guide to identify the tumor locations relevant for photothermal NIR irradiation.

Supplementary data to this article can be found online at <http://dx.doi.org/10.1016/j.jconrel.2015.05.280>.

## Acknowledgments

This work was supported by research grants from the Ministry of Science, ICT and Future Planning (NRF-2015R1A2A1A01005674), and from the Ministry of Trade, Industry & Energy (Technology Innovation Program, grant no. 10050648), Republic of Korea.

## References

- Z. Zhang, J. Wang, C. Chen, Near-infrared light-mediated nanoplatforms for cancer thermochemotherapy and optical imaging, *Adv. Mater.* 25 (2013) 3869–3880.

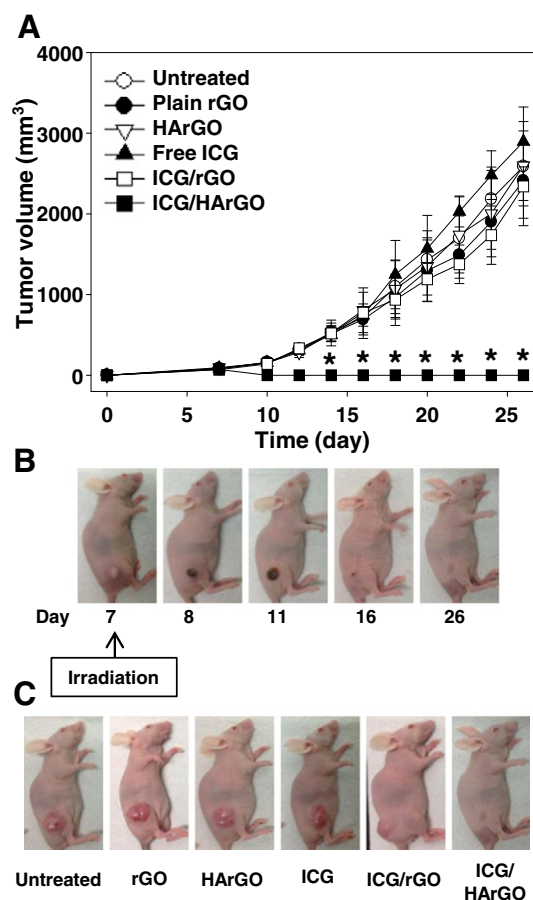


**Fig. 9.** Photothermal antitumor effect of ICG on nanosheets after image-guided irradiation. KB-bearing mice were intravenously treated with free ICG, rGO, ICG/rGO, HArGO, or ICG/HArGO by administering a single injection on day 6. After 24 h, the tumor tissues were irradiated with an 808-nm laser at a power density of 1.2 W/cm<sup>2</sup> for 3 min. (A) Tumor volumes, measured periodically using calipers until day 26. (B) The appearances of tumor sites in ICG/HArGO-treated mice, monitored starting on day 7. (C) The appearances of tumor sites in all groups, observed on day 26. \* $p < 0.05$  compared to other groups (ANOVA and Student–Newman–Keuls test;  $n = 5$ ).

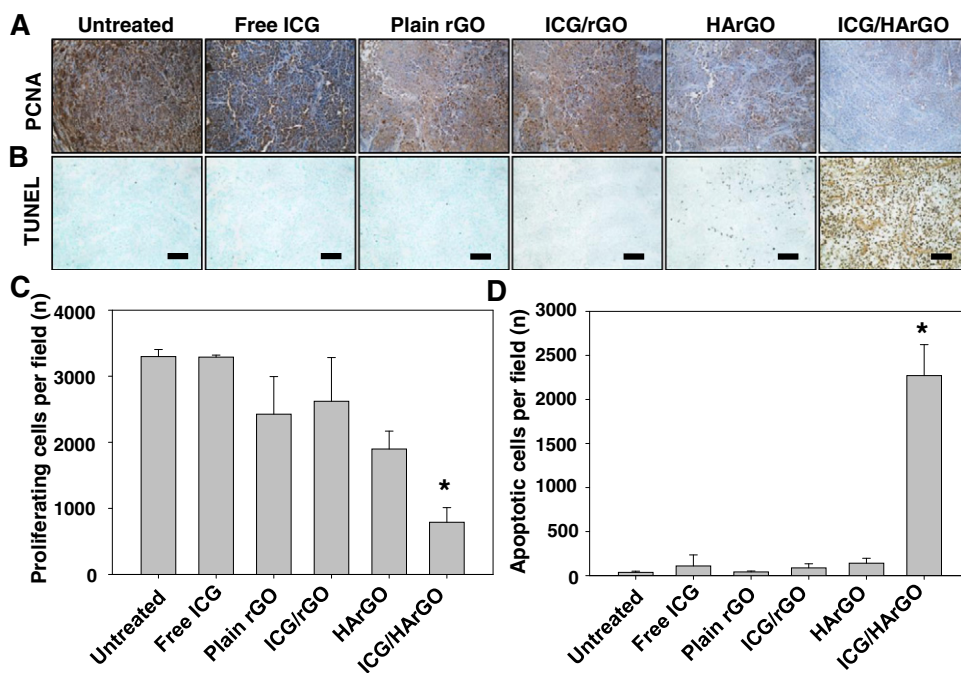


**Fig. 10.** Immunohistochemistry of tumor tissues treated with ICG. Tumor tissues were excised and sectioned for anti-PCNA antibody immunostaining (A) and TUNEL assay (B). The numbers of PCNA-immunostained (proliferating) cells (C) and TUNEL-labeled apoptotic cells (D) in isolated tumor tissues were determined. Scale bar = 100  $\mu$ m. \* $p < 0.05$  compared with other groups (ANOVA and Student–Newman–Keuls test;  $n = 5$ ).

- [2] C. Iancu, L. Mocan, Advances in cancer therapy through the use of carbon nanotube-mediated targeted hyperthermia, *Int. J. Nanomedicine* 6 (2011) 1675–1684.
- [3] W.I. Choi, J.Y. Kim, C.C. Byeon, Y.H. Kim, G. Tae, Tumor regression in vivo by photothermal therapy based on gold-nanorod-loaded, functional nanocarriers, *ACS Nano* 5 (2011) 1995–2003.
- [4] Y. Min, C.Q. Mao, S. Chen, G. Ma, J. Wang, Y. Liu, Combating the drug resistance of cisplatin using a platinum prodrug based delivery system, *Angew. Chem. Int. Ed.* 51 (2012) 6742–6747.
- [5] S.N. Goldberg, G.S. Gazelle, P.R. Mueller, Thermal ablation therapy for focal malignancy, *AJR Am. J. Roentgenol.* 174 (2000) 323–331.
- [6] A. Yuan, J. Wu, X. Tang, L. Zhao, F. Xu, Y. Hu, Application of near-infrared dyes for tumor imaging, photothermal, and photodynamic therapies, *J. Pharm. Sci.* 102 (2013) 6–28.
- [7] K. Namikawa, N. Yamazaki, Sentinel lymph node biopsy guided by indocyanine green fluorescence for cutaneous melanoma, *Eur. J. Dermatol.* 21 (2011) 184–190.
- [8] V. Saxena, M. Sadoqi, J. Shao, Degradation kinetics of indocyanine green in aqueous solution, *J. Pharm. Sci.* 92 (2003) 2090–2097.
- [9] E. Engel, R. Schraml, T. Maisch, K. Kobuch, B. König, R.M. Szeimies, J. Hillenkamp, W. Baumler, R. Vasold, Light-induced decomposition of indocyanine green, *Invest. Ophthalmol. Vis. Sci.* 49 (2008) 1777–1783.
- [10] T. Desmettre, J.M. Devoisselle, S. Mordon, Fluorescence properties and metabolic features of indocyanine green (ICG) as related to angiography, *Surv. Ophthalmol.* 45 (2000) 15–27.
- [11] B.M. Barth, S.S. Shanmugavelandy, J.M. Kaiser, D. Crespo-Gonzalez, N.A. DiVittore, C. McGovern, T.M. Goff, N.R. Keasey, J.H. Adair, T.P. Loughran Jr., D.F. Claxton, M. Kester, Targeted indocyanine-green-loaded calcium phosphosilicate nanoparticles for in vivo photodynamic therapy of leukemia, *ACS Nano* 5 (2011) 5325–5337.
- [12] Y. Ma, S. Tong, G. Bao, C. Gao, Z. Dai, Indocyanine green loaded SPIO nanoparticles with phospholipid-PEG coating for dual-modal imaging and photothermal therapy, *Biomaterials* 34 (2013) 7706–7714.
- [13] W.S. Kuo, Y.T. HAng, K.C. Cho, K.C. Chiu, C.H. Lien, C.S. Yeh, S.J. Chen, Gold nanomaterials conjugated with indocyanine green for dual-modality photodynamic and photothermal therapy, *Biomaterials* 33 (2012) 3270–3278.
- [14] H. Yang, H. Mao, Z. Wan, A. Zhu, M. Guo, Y. Li, X. Li, J. Wan, X. Yang, X. Shuai, H. Chen, Micelles assembled with carbocyanine dyes for theranostic near-infrared fluorescent cancer imaging and photothermal therapy, *Biomaterials* 34 (2013) 9124–9133.
- [15] J.T. Robinson, S.M. Tabakman, Y. Liang, H. Wang, H.S. Casalongue, D. Vinh, H. Dai, Ultrasmall reduced graphene oxide with high near-infrared absorbance for photothermal therapy, *J. Am. Chem. Soc.* 133 (2011) 6825–6831.
- [16] K. Yang, S. Zhang, G. Zhang, X. Sun, S.T. Lee, Z. Liu, Graphene in mice: ultrahigh in vivo tumor uptake and efficient photothermal therapy, *Nano Lett.* 10 (2010) 3318–3323.
- [17] W. Miao, G. Shim, S. Lee, Y.K. Oh, Structure-dependent photothermal anticancer effects of carbon-based photoreponsive nanomaterials, *Biomaterials* 35 (2014) 4058–4065.
- [18] D. Li, M.B. Müller, S. Gilje, R.B. Kaner, G.G. Wallace, Processable aqueous dispersions of graphene nanosheets, *Nat. Nanotechnol.* 3 (2008) 101–105.
- [19] W. Miao, G. Shim, C.M. Kang, S. Lee, Y.S. Choe, H.G. Choi, Y.K. Oh, Cholesteryl hyaluronic acid-coated, reduced graphene oxide nanosheets for anti-cancer drug delivery, *Biomaterials* 34 (2013) 9638–9647.
- [20] G. Shim, J.Y. Kim, J. Han, S.W. Chung, Y. Byun, Y.K. Oh, Reduced graphene oxide nanosheets coated with an anti-angiogenic anticancer lowmolecular-weight heparin derivative for delivery of anticancer drugs, *J. Control. Release* 189 (2014) 80–89.
- [21] F.M. Penha, E.B. Rodrigues, M. Maia, C.H. Meyer, P. Costa Ede, E. Dib, E. BeHara, A. Lourenco, A.A. Lima Filho, E.H. Freymuller, M.E. Farah, Biochemical analysis and decomposition products of indocyanine green in relation to solvents, dye concentrations and laser exposure, *Ophthalmologica* 230 (Suppl. 2) (2013) 59–67.
- [22] Y.W. Wang, Y.Y. Fu, Q. Peng, S.S. Guo, G. Liu, J. Li, H.H. Yang, G.N. Chen, Dye-enhanced graphene oxide for photothermal therapy and photoacoustic imaging, *J. Mater. Chem. B* 1 (2013) 5762–5767.
- [23] Y. Wang, Z. Li, J. Wang, J. Li, Y. Lin, Graphene and graphene oxide: biofunctionalization and applications in biotechnology, *Trends Biotechnol.* 29 (2011) 205–212.
- [24] A. Wojcik, P.V. Kamat, Reduced graphene oxide and porphyrin. An interactive affair in 2-D, *ACS Nano* 4 (2010) 6697–6706.
- [25] W. Miao, G. Shim, S. Lee, S. Lee, Y.S. Choe, Y.K. Oh, Safety and tumor tissue accumulation of pegylated graphene oxide nanosheets for co-delivery of anticancer drug and photosensitizer, *Biomaterials* 34 (2013) 3402–3410.
- [26] S.R. Dattir, M. Das, R.P. Singh, S. Jain, Hyaluronate tethered, “smart” multiwalled carbon nanotubes for tumor-targeted delivery of doxorubicin, *Bioconjug. Chem.* 23 (2012) 2201–2213.
- [27] M. Swierczewska, K.Y. Choi, E.L. Mertz, X. Huang, F. Zhang, L. Zhu, H.Y. Yoon, J.H. Park, A. Bhirde, S. Lee, X. Chen, A facile, one-step nanocarbon functionalization for biomedical applications, *Nano Lett.* 12 (2012) 3613–3620.
- [28] B.P. Shah, N. Pasquale, G. De, T. Tan, J. Ma, K.B. Lee, Core-shell nanoparticle-based peptide therapeutics and combined hyperthermia for enhanced cancer cell apoptosis, *ACS Nano* 8 (2014) 9379–9387.
- [29] D. Yoo, H. Jeong, C. Preihs, J. Choi, T.H. Shin, J.L. Sessler, J. Cheon, Double-effector nanoparticles: a synergistic approach to apoptotic hyperthermia, *Angew. Chem. Int. Ed. Engl.* 7 (2012) 12482–12485.
- [30] J. Zhou, J.K. Chen, Y. Zhang, Theoretical analysis of thermal damage in biological tissues caused by laser irradiation, *Mol. Cell. Biomech.* 4 (2007) 27–39.
- [31] R. Jiang, S. Cheng, L. Shao, Q. Ruan, J. Wang, Mass-based photothermal comparison among gold nanocrystals, PbS nanocrystals, organic dyes, and carbon black, *J. Phys. Chem. C* 117 (2013) 8909–8915.
- [32] M. Camerin, G. Jori, L. Della Ciana, S. Fabbri, S. Bonacchi, M. Montalti, L. Prodi, Photothermal sensitisation and therapeutic properties of a novel far-red absorbing cyanine, *Photochem. Photobiol. Sci.* 8 (2009) 1422–1431.